Journal of Power Sources 198 (2012) 251–257

Contents lists available at SciVerse ScienceDirect

Journal of Power Sources

journal homepage: www.elsevier.com/locate/jpowsour

Facile synthesis of porous $LiMn_2O_4$ spheres as positive electrode for high-power lithium ion batteries

Liu Jiang Xi [a], Hong-En Wang [a], Zhou Guang Lu [a,b], Shi Liu Yang [a], Ru Guang Ma [a], Jian Qiu Deng [a], C.Y. Chung [a,*]

[a] Department of Physics and Materials Science, City University of Hong Kong, Hong Kong Special Administrative Region
[b] College of Chemistry and Chemical Engineering, Central South University, Changsha, PR China

ARTICLE INFO

Article history:
Received 21 June 2011
Received in revised form
28 September 2011
Accepted 29 September 2011
Available online 5 October 2011

Keywords:
Manganese dioxide
Lithium manganate
Porous sphere
Lithium ion battery
High rate capability

ABSTRACT

A $LiMn_2O_4$ cathode material with novel porous spherical morphology exhibiting excellent electrochemical performance has been successfully prepared by using α-MnO_2 urchin-like structure as a self-sacrificial template. These cathode powders are characterized with X-ray powder diffractometry (XRD), field-emission scanning electron microscopy (FESEM), Brunauer–Emmett–Teller (BET) method and inductively coupled plasma emission spectrometry (ICP-AES). Furthermore, electrochemical properties have been studied by cyclic voltammetry (CV), electrochemical impedance spectroscopy (EIS) and charge/discharge cycling at various current rates. The results reveal that the porous $LiMn_2O_4$ spheres possess outstanding high rate capability and extremely high cycle stability at room temperature as well as elevated temperature. When tested at 10 C and 20 C rates, the first discharge capacities are up to 93.7 and 76.0 mAh g^{-1}. After 1000 cycles, the corresponding retention rates of capacities are more than 71% and 62% at room temperature. When cycled at 60 °C and 10 C rate, the first discharge capacity is 61.1 mAh g^{-1} between 3 and 4.5 V. After tested for 250 cycles at 60 °C, the retention rate of capacity is over 76%. This makes the porous $LiMn_2O_4$ cathode a promising candidate for high-power lithium ion batteries which may be used in demanding application such as electric vehicles.

1. Introduction

Rechargeable lithium ion batteries (LIBs) are one of the most promising energy storage devices for electric vehicles (EV) and hybrid electric vehicles (HEV), which possess high energy density, high power density, low cost, superior safety, and stable cycling lifespan. The spinel $LiMn_2O_4$ is generally considered as an excellent alternative to $LiCoO_2$ in power LIBs because it is inexpensive, safe and environmentally friendly [1–3]. However, its wide application in EV or HEV has been largely hindered by its poor rate capability and particular failure due to the dissolution of Mn into the electrolytes at elevated temperature [4]. The improvements of electrochemical reversibility and stability of spinel $LiMn_2O_4$ at high rate and elevated temperature for LIBs recently are becoming extremely challenging research topics for scientists and R&D engineers [5–9].

The capacity decay and poor cycling stability of $LiMn_2O_4$ cathode materials are mainly the detrimental consequences due to the dissolution of manganese in the electrolyte [10], the phase transition from cubic to tetragonal phase [11], and the changes of particle morphology or crystallinity [12,13]. Besides, the poor rate performance of bulk lithium ion electrode materials is primarily attributed to the very long distance for lithium ions to diffuse through the electrodes [14,15]. However, the transport distances of lithium ions in the solid can be considerably reduced due to the nanometer-sized powder electrode leading to much faster Li ion intercalation/deintercalation process [16,17]. Therefore, down-sizing of $LiMn_2O_4$ particles is of great help to improve the high-rate performance. Recently, spinel $LiMn_2O_4$ nanomaterials with various morphologies have been extensively prepared to improve their rate capabilities for LIBs, such as nanoparticles [18], nanotubes [19], nanowires [20], nanobelts [21], nanorods [22], and hollow nanospheres [23]. Single-crystalline nanotubes of spinel $LiMn_2O_4$ exhibit superior high rate capabilities and good cycling stability, and about 70% of its initial capacity can be retained after 1500 cycles at 5 C rate [19]. The high-quality single crystalline spinel $LiMn_2O_4$ nanowires showed high thermal stability and excellent cycle performance at high rate charge–discharge [20]. The $LiMn_2O_4$ nanorods showed a high charge storage capacity at high power rates compared with commercially available powders, and more than 85% of the initial charge storage capacity was maintained after over 100 cycles [22]. Besides, mesoporous $Li_{1.12}Mn_{1.88}O_4$ spinel showed higher rate capability relative to the corresponding bulk material (50% higher specific capacity

* Corresponding author. Tel.: +852 34427835; fax: +852 34420538.
E-mail address: appchung@cityu.edu.hk (C.Y. Chung).

0378-7753/$ – see front matter © 2011 Elsevier B.V. All rights reserved.
doi:10.1016/j.jpowsour.2011.09.100

at a rate of 30 C, 3000 mA g^{-1}) at ambient temperature with good stability at elevated temperatures, and without the need for deliberate coating or doping with foreign ions [24]. Hollow microspheres of $LiMn_2O_4$ have been synthesized and used as a cathode material in lithium ion batteries, which showed that hollow microspheres of $LiMn_2O_4$ exhibited better rate capability than the solid microspheres [25]. Therefore, it can be concluded that the electrochemical performance of $LiMn_2O_4$ electrodes appreciably depends on the morphology, the crystalline phase, and the porosity of the structure.

Usually, electrodes made of sub-micron size spherical particles show higher volumetric energy density compared with irregular shaped nanoparticles. It is because microsized spherical particles can easily be packed attaining relatively higher tap density [26]. However, the micron solid spheres have longer ion and electron transportation distance as compared with nanoparticles because the electrolyte cannot penetrate into the internal volume of the solid spheres easily. Hence, an ideal structure for $LiMn_2O_4$ with both high volumetric energy density and high rate capability should be a porous microsphere consisted of nanocrystallites tightly compacted to form three-dimensional channels for ion diffusion. On one hand the porous microsphere can increase the interfacial area between microsphere and electrolyte; on the other hand it might lead to possible increase in the dissolution of Mn^{3+} into the electrolyte. However, lithium-rich compositions within the $Li_{1+x}Mn_{2-x}O_4$ system ($0 < x \leq 0.33$) could exhibit good cycling performance, which can be attributed to the high average oxidation state and the presence of less soluble Mn^{3+}, but at the same time compromising the energy storage capacity [24,27–29]. But, high rate capability becomes even more important to ensure high utilization of the reduced theoretical capacity [24]. Porous $LiMn_2O_4$ spheres have been synthesized by ultrasonic spray pyrolysis method [7,30–32]. In particular, Zhang et al. [30] reported that porous $LiMn_2O_4$ spheres prepared by a single-step ultrasonic spray pyrolysis method could deliver excellent rate performance about 100 mAh g^{-1} at 10 C and Ni substitution could contribute to improving electrochemical performances in the voltage range of 4.95–3.5 V.

In this paper, we reported the synthesis of spinel lithium-rich $LiMn_2O_4$ porous spheres (LMO-PS) by a facile solid-state reaction method using urchin-like α-MnO_2 structure as a self-sacrificial template. Moreover, we compared the electrochemical performances of LMO-PS with those of lithium-rich $LiMn_2O_4$ partly porous spheres (LMO-PP) and total lithium-rich $LiMn_2O_4$ solid spheres (LMO-SS), which revealed that LMO-PS had the best rate performance and cycling stability.

2. Experimental

2.1. Synthesis

2.1.1. Synthesis of α-MnO_2 urchin-like structures

Analytical grade $MnSO_4{\cdot}H_2O$, $AgNO_3$, $Na_2S_2O_8$, and deionized water were used to prepare α-MnO_2 urchin-like structures via a homogeneous catalytic route as reported elsewhere [33] with some modifications. All chemicals were used without further purification. In a typical synthesis, 0.4 mmol $MnSO_4{\cdot}H_2O$ and 0.4 mmol $Na_2S_2O_8$ were mixed in 100 mL distilled water at room temperature. Then 4 mL 0.059 mmol L^{-1} of $AgNO_3$ solution was added. After the homogeneous solution was settled for 2 days at room temperature, the precipitate was collected and washed with absolute ethanol and distilled water for several times. Subsequently, the powders were dried in a vacuum.

2.1.2. Synthesis of spherical $MnCO_3$ spheres

The synthesis method of spherical $MnCO_3$ spheres was similar to previous report [25]. 1 mmol $MnSO_4{\cdot}H_2O$ and 2 mmol of $NaHCO_3$ were separately dissolved in 70 mL distilled water. Then, 7 mL ethanol was added to the $MnSO_4$ solution under stirring, and the $NaHCO_3$ solution was then directly added. The resulting mixture was left at room temperature for 3 h to precipitate. The as-prepared $MnCO_3$ solid microspheres were collected, washed with distilled water and absolute alcohol several times, and then dried in a vacuum.

2.1.3. Synthesis of α-MnO_2 burr-like microspheres

The synthesis of α-MnO_2 burr-like microspheres was reported elsewhere [34] and similar to the method described in Section 2.1.1. The difference is that H_2SO_4 (98 wt.%, 4 mL) was added to the mixture of $MnSO_4{\cdot}H_2O$ and $Na_2S_2O_8$ (0.4 mmol) solution.

2.1.4. Synthesis of LMO-PS, LMO-PP and LMO-SS

As-prepared α-MnO_2 urchin-like structures, $MnCO_3$ microspheres and α-MnO_2 burr-like microspheres were mixed with $LiOH{\cdot}H_2O$ with the molar ratio of 1.2:2 independently. They were then dispersed into 2 mL ethanol, ground to form a fine mixture, dried at room temperature, and then calcined at 800 °C in atmospheric condition for 10 h. The LMO-PS, LMO-PP and LMO-SS were prepared, respectively.

2.2. Characterization of the as-prepared samples

The crystalline structures of the as-prepared products were characterized by X-ray diffraction (XRD) technique using a Siemens X-ray diffractometer with Cu Kα radiation. Specific surface area and average pore size were determined by nitrogen adsorption–desorption isotherms at 77 K using a NOVA 1200e Surface Area & Pore Size Analyzer (Quantachrome Instruments). The element composition of the as-prepared product was analyzed by inductively coupled plasma emission spectrometry (ICP-AES, ICPE 9000 Shimadzu). The morphologies of the as-prepared products were examined by a field-emission SEM (Hitachi S4800).

2.3. Electrochemical performance measurement

The electrochemical properties of the products were analyzed by making CR2025 coin-type cells with lithium metal as the negative electrode. The cathode slurry was prepared by mixing the active material, acetylene black and polyvinylidene fluoride (PVDF) in the weight ratio of 70:20:10. The blended slurry was then cast onto an aluminum foil current collector and dried at 120 °C for 10 h in a vacuum oven. Then, circular (1.6 cm^2) cathode discs were punched from the aluminum foil. The punched cathodes were weighed to determine the amount of active materials (typically about 6 mg) before being loaded into coin-type cells. The cell was assembled in a glove box filled with high purity argon gas with low concentration of oxygen and low humidity. The electrolyte composed of 1 M $LiPF_6$ dissolved in ethylene carbonate (EC)/dimethyl carbonate (DMC) (1:1 in volume). Galvanostatic charge/discharge experiments were performed between 3.0 and 4.5 V at different current densities (1 C rate corresponds to the current density of 148 mA g^{-1}). Electrochemical impedance spectroscopy (EIS) and cyclic voltammetry (CV) analyses were recorded on a Zahner IM6 electrochemical station. The amplitude of the AC signal was 5 mV over the frequency range between 100 kHz and 0.01 Hz. The sweep potential range of CV is between 3.5 and 4.5 V.

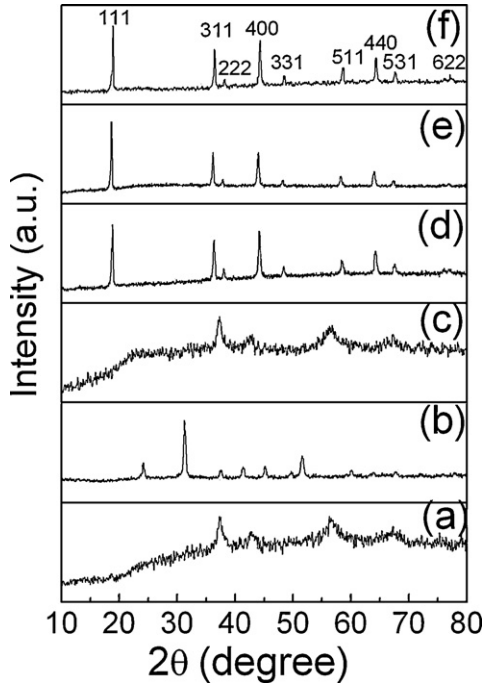

Fig. 1. XRD patterns of (a) MnO_2 urchin-like microspheres, (b) $MnCO_3$ microspheres, (c) MnO_2 burr-like microspheres, (d) LMO-PS, (e) LMO-PP and (f) LMO-SS.

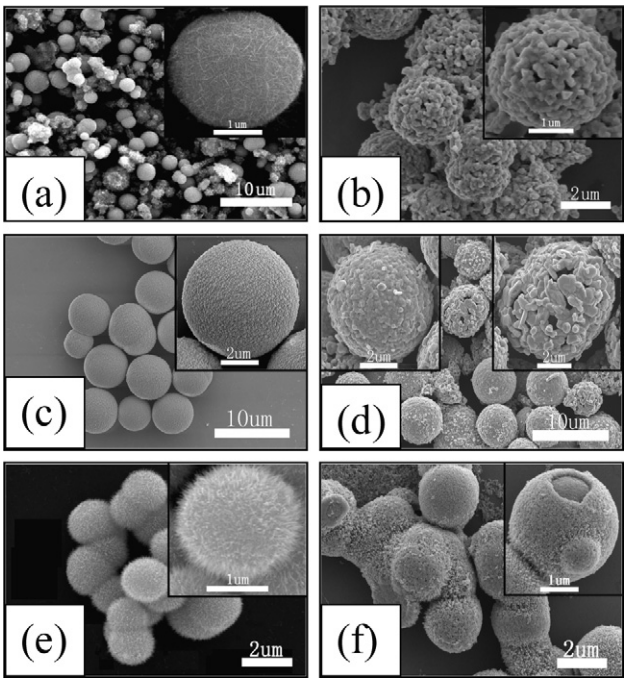

Fig. 2. FESEM images of (a) MnO_2 urchin-like microspheres, (b) $LiMn_2O_4$ porous spheres (LMO-PS), (c) $MnCO_3$ microspheres, (d) $LiMn_2O_4$ spheres consisting of partly porous spheres and solid spheres (LMO-PP), (e) MnO_2 burr-like microspheres and (f) $LiMn_2O_4$ solid spheres (LMO-SS).

3. Results and discussion

Fig. 1(a)–(f) shows the XRD patterns of MnO_2 urchin-like microspheres, $MnCO_3$ microspheres, MnO_2 burr-like microspheres, LMO-PS, LMO-PP and LMO-SS, respectively. The spectra of Fig. 1(a) and (c) can be indexed as the pure tetragonal α-MnO_2 phase (JCPDS 44-0141). Fig. 1(b) can be indexed as the pure $MnCO_3$ phase (JCPDS 44-1472). The reflections of Fig. 1(d)–(f) can be indexed as spinel $LiMn_2O_4$ structure (JCPDS 35-0782). Peak shift occurs for $LiMn_2O_4$ spheres, which results from the change of lattice parameters. Gummow et al. [27] reported that the lattice constants of $Li_{1+\delta}Mn_{2-\delta}O_4$ ($0 < \delta \leq 0.33$) decrease with the increase of lithium content, and the manganese ions in the octahedral (16d) sites were replaced by lithium ions with a concomitant increase in the manganese-ion oxidation state to maintain charge neutrality. According to the XRD patters, no other chemical compositions were found.

The particle size and morphology of samples and their precursors are shown in Fig. 2. From Fig. 2(a) and (b), it can be seen that the precursor MnO_2 particles are urchin-like microspheres, and the corresponding $LiMn_2O_4$ particles are porous spheres with diameter of about 2 μm, which are made up of some nanoparticles with the size below 100 nm. Fig. 2(c) and (d) shows the precursor $MnCO_3$ particles which are microspheres, and the corresponding $LiMn_2O_4$ microspheres are composed of solid spheres and porous spheres, and the average particle size is around 5 μm. Moreover, Fig. 2(e) and (f) shows that the precursor MnO_2 particles look burr microspheres, and the corresponding $LiMn_2O_4$ spheres are totally solid spheres with the size of about 2 μm.

The BET surface areas of the LMO-PS, LMO-PP and LMO-SS samples have been determined to be 17.73, 13.83 and 5.42 $m^2\,g^{-1}$, respectively. And the corresponding average pore sizes of LMO-PS, LMO-PP and LMO-SS samples are calculated to be 3.11, 2.53 and 1.15 nm, respectively.

The relationship between discharge capacities and rates of LMO-PS is shown in Fig. 3. It can be seen that the discharge capacities of LMP-PS are not favorable at low current rates, i.e., 0.1 C and 1 C, as compared with the literature [24]. The reason is that lithium-rich

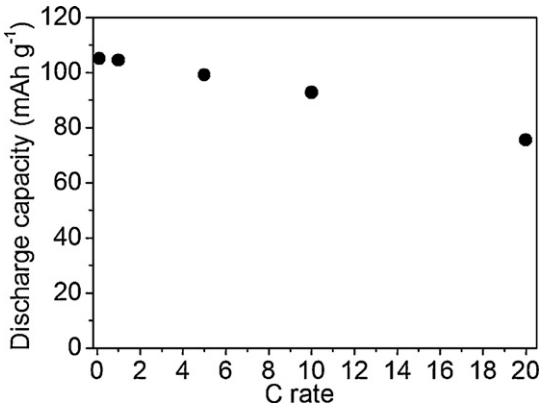

Fig. 3. The relationship between discharge capacities and rates of porous $LiMn_2O_4$ microspheres (LMO-PS).

compositions within the $LiMn_2O_4$ system can compromise theoretical capacity. The ICP-AES results in Table 1 indicate that the lithium is rich within LMO-PS product, of which the compositions are basically consistent with the designed composition. However, the excellent high rate capabilities at 5 C, 10 C and 20 C are very attractive, which can be attributed to the porous structure which favors fast lithium ion diffusion.

The first charge and discharge curves of LMO-PS, LMO-PP and LMO-SS at the rates of 10 C and 20 C are shown in Fig. 4(a) and (b). The first discharge capacities of LMO-PS, LMO-PP and LMO-SS are 93.7, 79.7 and 34.5 mAh g^{-1} at 10 C rate, and 76.0, 19.4 and 0.7 mAh g^{-1} at 20 C rate, respectively. It is obvious that the

Table 1
The ICP-AES results of LMO-PS sample.

Sample	C_{Li} (mol L^{-1})	C_{Mn} (mol L^{-1})	Molar ratio of Mn to Li
LMO-PS	3.45×10^{-4}	5.66×10^{-4}	1.21:2

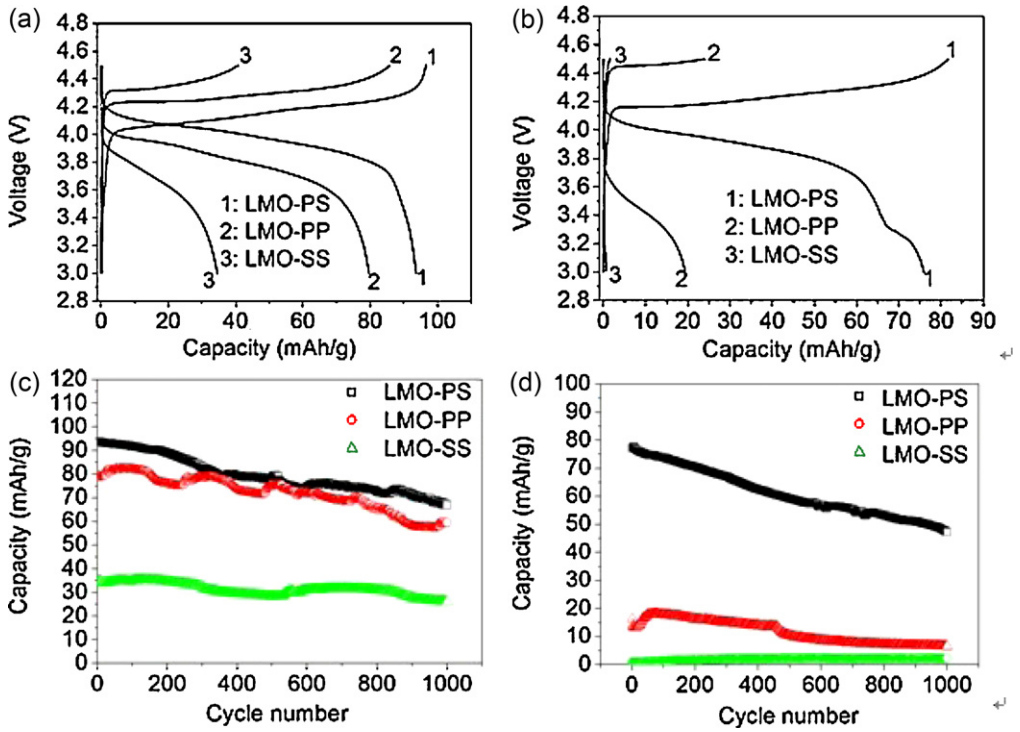

Fig. 4. The first charge and discharge curves of LMO-PS, LMO-PP, and LMO-SS at the rate of (a) 10 C and (b) 20 C; cycling performance of LMO-PS, LMO-PP and LMO-SS at the rate of (c) 10 C and (d) 20 C.

LMO-PS has much better high rate capability than that of LMO-PP and LMO-SS. Moreover, the discharge capacities of LMO-PP and LMO-SS decrease quickly with the increase of discharge rate from 10 C to 20 C, while the LMO-PS still has high rate capability at 20 C rate. The excellent high rate capability for LMO-PS maybe due to its porous morphology consisted of nanocrystallites tightly compacted to form three-dimensional channels which are extraordinarily suitable for lithium ion diffusion. Fig. 4(c) and (d) reveals the cycle performance of samples at 10 C and 20 C rates. It can be seen that the discharge capacity of LMO-PS is always biggest at high rates.

After 1000 cycles at 10 C and 20 C rates, the discharge capacities of LMO-PS are 66.7 and 47.4 mAh g^{-1}, respectively. The corresponding retention rates of capacities are 71% and 62% at room temperature, as shown in Fig. 5. The excellent cycle property of LMO-PS has a strong correlation with the porous structure which has increased the lithium ion diffusion; on the other hand, the lithium-rich compositions can also lead to high average oxidation state thus decreasing the presence of soluble Mn^{3+} [24,27–29]. The concerted effects due to the choice of morphology and composition are believed to be the contributing factors for the improvement in electrochemical performance.

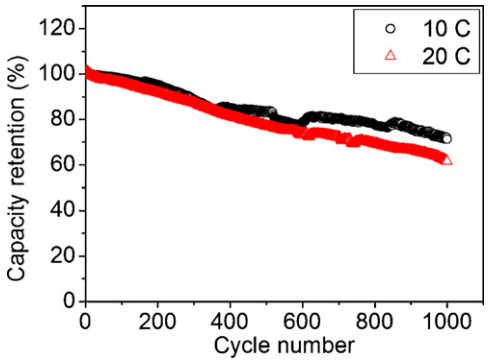

Fig. 5. The capacity retention of LMO-PS with respect to the cycle number at 10 and 20 C rates.

Fig. 6(a)–(c) shows the cyclic voltammograms of the LMO-PS, LMO-PP and LMO-SS at different scan rates, which reveals that the peak current increases with the increase of scan rates. Moreover, the peak currents of LMO-SS, LMO-PP and LMO-PS increase in sequence at the same scan rate, which implies that the internal resistance of LMO-PS cathode is the smallest and the diffusion rate of Li^+ is the fastest. In Fig. 6(d), the plotting of the peak currents vs. the square root of the scan rates of each sample shows a beautiful linear relationship, which suggests that lithium insertion in LMO particle is a diffusion-controlled process. For a reversible reaction involving Li-ion diffusion behavior, the chemical diffusion coefficient of Li-ion can be obtained by the Randles–Sevcik equation [35]:

$$i_p = 0.4463 z^{3/2} F^{3/2} C_{Li} A R^{-1/2} T^{-1/2} D_{Li}{}^{1/2} v^{1/2} \quad (1)$$

where i_p being the peak current value (A), z being the charge transfer number (for lithium ion $z=1$), F being the Faraday's constant (96,485 C mol^{-1}), C_{Li} being the Li-ion concentration (0.0238 mol cm^{-3} for $LiMn_2O_4$ derived from the theoretical density of 4.3 g cm^{-3}), A being the surface area of electrode (cm^2), R being the universal gas constant (8.314 J mol^{-1} K^{-1}), T being the absolute temperature (K), D_{Li} being the chemical diffusion coefficient (cm^2 s^{-1}), and v being the scanning rate (V s^{-1}). The anodic chemical diffusion coefficients of Li-ion in LMO-PS, LMO-PP and LMO-SS electrodes calculated by foregoing Eq. (1) with the slope of the i_p vs. $v^{1/2}$ plot are listed in Table 2. The analysis reveals that the chemical diffusion coefficients of LMO-PS, LMO-PP and LMO-SS are

Table 2
The chemical diffusion coefficient of samples.

Sample	LMO-PS	LMO-PP	LMO-SS
D_{Li} (cm^2 s^{-1})	4.98×10^{-8}	2.57×10^{-8}	3.62×10^{-9}

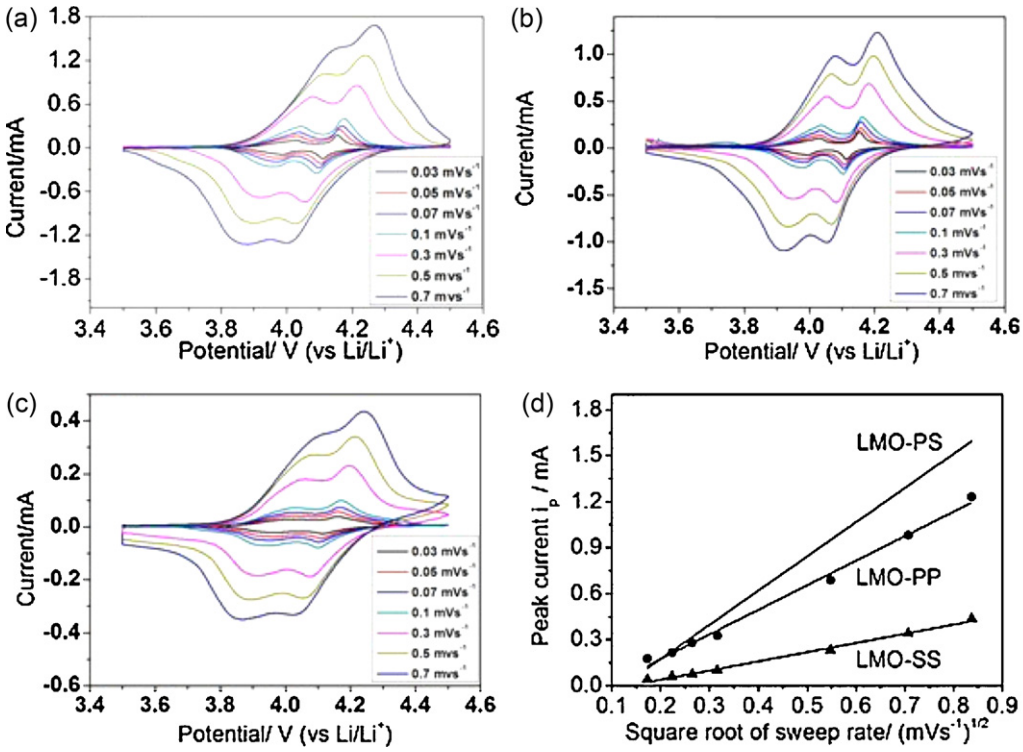

Fig. 6. Cyclic voltammograms of the (a) LMO-PS, (b) LMO-PP, and (c) (LMO-SS) at different scan rates; (d) the plotting of peak current (around 4.17 V) vs. square root of the scan rate for different samples.

4.98×10^{-8}, 2.57×10^{-8} and 3.62×10^{-9} $cm^2\ s^{-1}$, respectively. The chemical diffusion coefficient increases with the increases of the BET surface area. The LMO-PS has highest chemical diffusion coefficient which concurs the proposal that porous morphology of the LMO-PS is very favorable for lithium ion diffusion. This infers that the chemical diffusion coefficient is closely related to the unique porous structure.

Fig. 7 shows the electrochemical impedance spectra (EIS) of the batteries after activation. The impedance spectra consisted of two depressed semicircles in high-to-medium frequency region and a straight line in low frequency region. In high frequency region, an intercept at the Z_{real} axis corresponds to the ohmic resistance (R_s) and the semicircle correlates closely to the Li-ion migration resistance (R_f) through the multilayer surface films. The semicircle in the middle frequency range is related to the charge transfer resistance (R_{ct}) and the inclined line at low frequency region represents the Warburg impedance (Z_ω), which is associated with lithium-ion diffusion in the $LiMn_2O_4$ particles [10]. The parameters of impedance spectra were simulated by ZSIMPWIN software and the spectra have been fitted with an equivalent circuit as shown in the inset of Fig. 7(b). The fitted parameters are summarized in Table 3. From Table 3, it can be seen that these three samples have a similar R_s value of ~2.73 Ω, and the LMO-SS displays larger R_f and R_{ct} values than those of LMO-PS and LMO-PP. The Warburg coefficients (σ) can be considered as a resistance barrier for lithium ion diffusion because it is inversely proportional to the diffusion coefficient of lithium ion in the electrode. The conventional Warburg impedance (Z_ω) formula [36] is shown as follows:

$$Z_\omega = \sigma(1-j)\omega^{-1/2}, \quad |Z'| = A_r\omega^{-1/2}, \quad |Z''| = A_i\omega^{-1/2},$$
$$\sigma = \frac{A_r + A_i}{2} \tag{2}$$

where σ being the Warburg coefficient, j being the square root of -1, ω being the angular frequency, $|Z'|$ being the real resistance, $|Z''|$ being the imaginary resistance, A_r being the Warburg coefficient of real part and A_i being the Warburg coefficient of imaginary part. According to the formula, the Warburg coefficient of real part and imaginary part can be obtained from the slope of the $|Z'|$ vs. $\omega^{-1/2}$ and $|Z''|$ vs. $\omega^{-1/2}$, respectively. Fig. 7(c)–(e) reveals the linear relationship of $|Z'|$ vs. $\omega^{-1/2}$ and $|Z''|$ vs. $\omega^{-1/2}$ for LMO-PS, LMO-PP and LMO-SS cells. The A_r and A_i in LMO-PS, LMO-PP and LMO-SS electrodes are separately 83.69 and 81.29, 110.24 and 117.93, 354.21 and 362.71, respectively, which were calculated by Eq. (2) with the slope of the $|Z'|$ vs. $\omega^{-1/2}$ and $|Z''|$ vs. $\omega^{-1/2}$ plot as listed in Table 3. Moreover, Warburg coefficients (σ) were also calculated in LMO-PS, LMO-PP and LMO-SS electrodes and the value is 82.49, 114.09 and 358.46, respectively. It reveals that Warburg coefficient decreases with the increases of the BET surface area. The LMO-PS electrode has the smallest Warburg coefficient as compared with the LMO-PP and LMO-SS samples. This observation clearly demonstrates the superiority of a porous structure on enhancing the lithium ion transportation, leading to much improved high rate capability. This result is consistent with the aforementioned cyclic voltammetry (CV) analyses.

Fig. 8(a) reveals the cycle performance of LMO-PS at 25, 40, 50 and 60 °C at 10 C rate between 3 and 4.5 V, and first discharge capacities are 93.7, 73.3, 68.3 and 61.1 mAh g^{-1}, respectively. After 250 cycles, the discharge capacities still maintain at 86.5, 67.6, 59.0 and 46.7 mAh g^{-1}, and the retention rates of capacities are 92.3, 92.3, 86.4 and 76.4% at 25, 40, 50 and 60 °C at 10 C rate between 3 and 4.5 V, respectively. It can be concluded that the LMO-PS possesses

Table 3
The fitted and calculated electrochemical impedance parameters of the three samples.

Sample	R_s (Ω)	R_f (Ω)	R_{ct} (Ω)	A_r	A_i	σ
LMO-PS	2.77	8.91	88.53	83.69	81.29	82.49
LMO-PP	2.97	6.98	80.43	110.24	117.93	114.09
LMO-SS	2.44	14.59	134.40	354.21	362.71	358.46

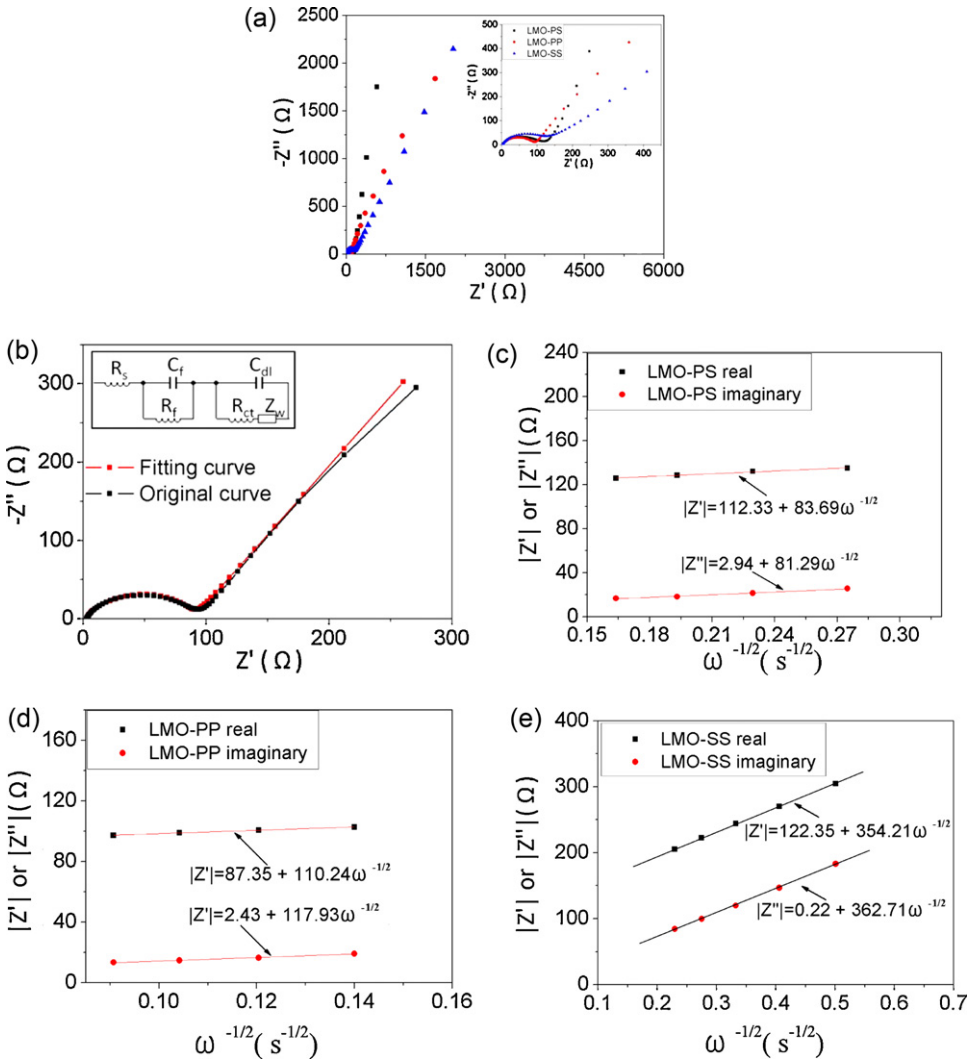

Fig. 7. (a) Electrochemical impedance spectra of the LMO-PS, LMO-PP, and LMO-SS samples; (b) the original and fitting EIS curves of the LMO-PP sample; (c–e) the plotting of real resistance and imaginary resistance vs. inverse square root of the angular frequency of the three samples: (c) LMO-PS; (d) LMO-PP; (e) LMO-SS.

exceptionally high temperature electrochemical stability at high rate, which maybe attributed to the good crystallinity and lithium richness of samples. The observed capacity decrease with increasing temperature is mainly caused by the dissolution of Mn from the spinel material into the electrolyte, especially above 50 °C. The dissolution of Mn is generally attributed to the formation of HF when $LiPF_6$ is used as the electrolyte salt [10].

The typical CV plots of LMO-PS/Li coin cell after cycled at 10 C rate for different cycles at a scan rate of 0.1 mV s^{-1} in a potential range of 3.5–4.5 V are shown in Fig. 9. As depicted in

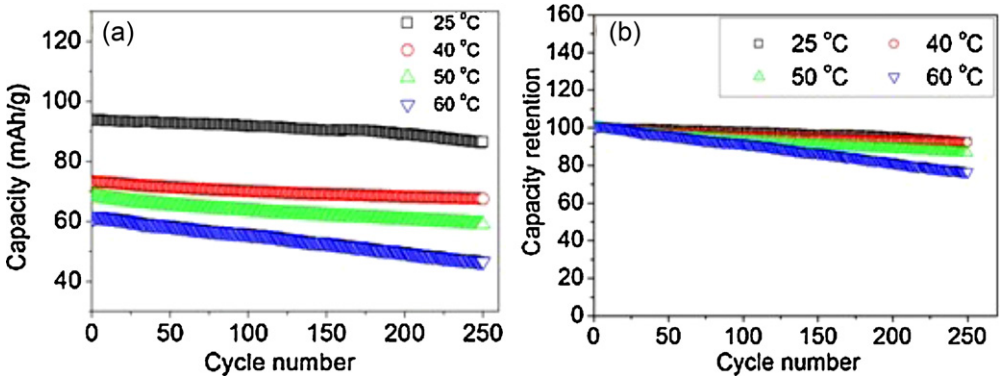

Fig. 8. (a) The cycle performance of LMO-PS at different temperatures at 10 C rate between 3 and 4.5 V; (b) the capacity retention of LMO-PS with the cycle number at different temperatures at 10 C rate between 3 and 4.5 V.

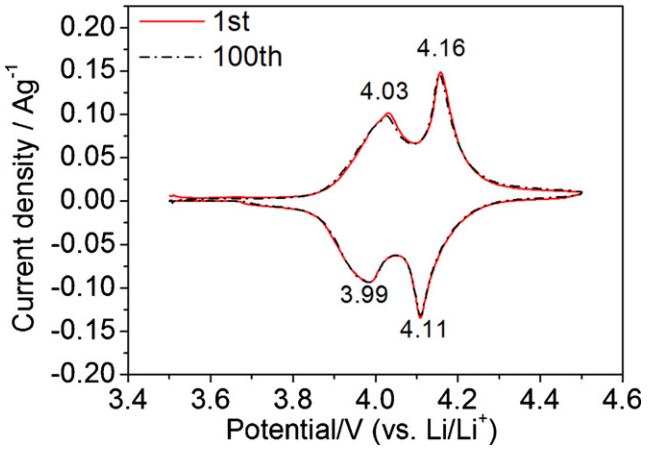

Fig. 9. CV plots (0.1 mV s^{-1}) of LMO-PS electrode between 3.5 and 4.5 V vs. Li/Li^+ after cycling at 10 C rate for different cycles.

Fig. 9, two couples of clearly separated sharp oxidation peaks located at 4.03 and 4.16 V and the corresponding reduction peaks located at 4.11 and 3.99 V (vs. Li/Li^+) for LMO-PS can be observed and no obvious difference can be seen between the voltage profiles after 1 cycle and those after 100 cycles. This infers that LMO-PS electrodes remain superior in terms of lithium ion intercalation/deintercalation reversibility. The first oxidation peak is attributed to lithium ion removal from one half of the tetrahedral sites in the spinel and the second one to the removal of residual lithium ion from the remaining tetrahedral sites [37]. Moreover, the difference between anodic and cathodic peak positions is only 50 mV and 40 mV, respectively, also suggesting good reversibility of the cathode that may facilitate lithium ion insertion/deinsertion into/from the spinel matrix. Furthermore, high-symmetric redox peaks are still retained for the 100th cycle at 10 C rate. Therefore, it is estimated that the LMO-PS is stable enough to sustain the charge/discharge cycling without evident structural deformation or destruction at 10 C rate, suggesting its excellent high rate property for LIBs.

4. Conclusions

Lithium-rich $LiMn_2O_4$ porous spheres were successfully prepared using urchin-like α-MnO_2 microspheres as self-sacrificial template and extensively characterized as cathode materials for lithium ion batteries. The results show that the spherical porous particles possess exceptional high rate charge/discharge capability and are extremely stable upon electrochemical cycling. The lifespan was much longer than that of the partly porous $LiMn_2O_4$ spheres as well as the solid $LiMn_2O_4$ microspheres. Moreover, the as-prepared lithium-rich $LiMn_2O_4$ porous spheres exhibited very good electrochemical properties at high discharge rate under high temperature. Therefore, the porous lithium-rich $LiMn_2O_4$ microspheres have great potential in application as cathode material for next-generation high-power lithium ion batteries.

Acknowledgements

This work was financially supported by the GRF Grant (#9041528, CityU 100510) from the Hong Kong SAR government Research Grant Council. Z.G.L. would like to thank the support from the National Natural Science Foundation of China (No. 21001117/B0107). The authors also thank Dr Hua Cheng and Miss Ling-Xia Zheng for their help in BET analyses.

References

[1] A.S. Aricò, P. Bruce, B. Scrosati, J.M. Tarascon, W.V. Schalkwijk, Nat. Mater. 5 (2005) 366–377.
[2] P.G. Bruce, B. Scrosati, J.M. Tarascon, Angew. Chem. Int. Ed. 47 (2008) 2930–2946.
[3] G. Amatucci, J.M. Tarascon, J. Electrochem. Soc. 149 (2002) K31–K46.
[4] M.S. Whittingham, Chem. Rev. 104 (2004) 4271–4301.
[5] H.W. Lee, P. Muralidharan, R. Ruffo, C.M. Mari, Y. Cui, D.K. Kim, Nano Lett. 10 (2010) 3852–3856.
[6] M. Okubo, Y. Mizuno, H. Yamada, J. Kim, E. Hosono, H.S. Zhou, T. Kudo, I. Honma, ACS Nano 4 (2010) 741–752.
[7] I. Taniguchi, Ind. Eng. Chem. Res. 44 (2005) 6560–6565.
[8] M.W. Raja, S. Mahanty, R.N. Basu, J. Mater. Chem. 19 (2009) 6161–6166.
[9] H. Uchiyama, E. Hosono, H.S. Zhou, H. Imai, J. Mater. Chem. 19 (2009) 4012–4016.
[10] Y. Liu, X. Li, H. Guo, Z. Wang, Q. Hu, W. Peng, Y. Yang, J. Power Sources 189 (2009) 721–725.
[11] M.M. Thackeray, J. Am. Ceram. Soc. 82 (1999) 3347–3354.
[12] T. Doi, M. Inaba, H. Tsuchiya, S.K. Jeong, Y. Iriyama, T. Abe, Z. Ogumi, J. Power Sources 180 (2008) 539–545.
[13] Y.G. Mateyshina, U. Lafont, N.F. Uvarov, E.M. Kelder, Russ. J. Electrochem. 45 (2009) 602–605.
[14] Y. Wang, G.Z. Cao, Adv. Mater. 20 (2008) 2251–2269.
[15] Y.G. Guo, Y.S. Hu, W. Sigle, J. Maier, Adv. Mater. 19 (2007) 2087–2091.
[16] X.W. Lou, Y. Wang, C.L. Yuan, J.Y. Lee, L.A. Archer, Adv. Mater. 18 (2006) 2325–2329.
[17] H.E. Wang, H. Cheng, C.P. Liu, X. Chen, Q.L. Jiang, Z.G. Lu, Y.Y. Li, C.Y. Chung, W.J. Zhang, J.A. Zapien, L. Martinu, I. Bello, J. Power Sources 196 (2011) 6394–6399.
[18] C.J. Curtis, J.X. Wang, D.L. Schulz, J. Electrochem. Soc. 151 (2004) A590–A598.
[19] Y.L. Ding, J. Xie, G.S. Cao, T.J. Zhu, H.M. Yu, X.B. Zhao, Adv. Funct. Mater. 21 (2010) 348–355.
[20] E. Hosono, T. Kudo, I. Honma, H. Matsuda, H.S. Zhou, Nano Lett. 9 (2009) 1045–1051.
[21] L.Z. Zhang, J.C. Yu, A.W. Xu, Q. Li, K.W. Kwong, L. Wu, Chem. Commun. (2003) 2910–2911.
[22] D.K. Kim, P. Muralidharan, H.W. Lee, R. Ruffo, Y. Yang, C.K. Chan, H.L. Peng, R.A. Huggins, Y. Cui, Nano Lett. 8 (2008) 3948–3952.
[23] J.Y. Luo, H.M. Xiong, Y.Y. Xia, J. Phys. Chem. C 112 (2008) 12051–12057.
[24] F. Jiao, J.L. Bao, A.H. Hill, P.G. Bruce, Angew. Chem. Int. Ed. 47 (2008) 9711–9716.
[25] X.L. Xiao, J. Lu, Y.D. Li, Nano Res. 3 (2010) 733–737.
[26] J.F. Qian, M. Zhou, Y.L. Cao, X.P. Ai, H.X. Yang, J. Phys. Chem. C 114 (2010) 3477–3482.
[27] R.J. Gummow, A. de Kock, M.M. Thackeray, Solid State Ionics 69 (1994) 59–67.
[28] K. Ariyoshi, E. Iwata, M. Kuniyoshi, H. Wakabayashi, T. Ohzuku, Electrochem. Solid-State Lett. 9 (2006) A557–A560.
[29] Z.H. Chen, K. Amine, J. Electrochem. Soc. 153 (2006) A1279–A1283.
[30] L.Q. Zhang, T. Yabu, I. Taniguchi, Mater. Res. Bull. 44 (2009) 707–713.
[31] Z. Bakenov, I. Taniguchi, Solid State Ionics 176 (2005) 1027–1034.
[32] I. Taniguchi, Z. Bakenov, Powder Technol. 159 (2005) 55–62.
[33] Z.Q. Li, Y. Ding, Y.J. Xiong, Y. Xie, Cryst. Growth Des. 5 (2005) 1953–1958.
[34] Z.Q. Li, Y. Ding, Y.J. Xiong, Q. Yang, Y. Xie, Chem. Commun. (2005) 918–920.
[35] J. Xie, N. Imanishi, A. Hirano, M. Matsumura, Y. Takeda, O. Yamamoto, Solid State Ionics 178 (2007) 1218–1224.
[36] R. Greef, R. Peat, L.M. Peter, et al., Instrumental Methods in Electrochemistry, John Wiley &Sons, Inc., New York, 1986, p. 265.
[37] M.M. Thackeray, W.I.F. David, P.G. Bruce, J.B. Goodenough, Mater. Res. Bull. 18 (1983) 461–472.